Non-Fermi-liquid signatures of quadratic band touching and phonon anomalies in metallic $Pr_2Ir_2O_7$

M. Rosalin [1], Prachi Telang,[2] Surjeet Singh,[2] D. V. S. Muthu [1], and A. K. Sood [1,*]

[1]*Department of Physics, Indian Institute of Science, Bangalore 560012, India*
[2]*Department of Physics, Indian Institute of Science Education and Research, Pune, Maharashtra 411008, India*

A single Fermi node in $Pr_2Ir_2O_7$ protected by time reversal and inversion symmetry resulting from an interplay between strong electronic correlations and spin-orbit coupling (SOC) has attracted significant attention. Here, we report a detailed temperature-dependent Raman study of the "quadratic band touching Luttinger semimetal" $Pr_2Ir_2O_7$. In addition to phonons, we observe an underlying flat electronic continuum due to electronic Raman scattering (ERS) that is dominant below a characteristic temperature T_Q. The observed ERS is understood using the Raman susceptibility of a non-Fermi liquid expected in a quadratic band touching system. The phonon frequencies and linewidths show anomalous temperature dependence below $T_Q \sim 150$ K attributed to strong electron-phonon coupling (EPC) in a quadratic band touching (QBT) state. The Ir-O-Ir bending E_g mode shows pronounced Fano asymmetry as well as anomalous linewidth broadening below T_Q. Further, a Raman line at ~ 460 cm^{-1} involving crystal field transition couples strongly to the T_{2g} phonon at ~ 350 cm^{-1}. Our results establish the enhanced scale of electron-electron correlations and electron-phonon coupling in the QBT state of metallic $Pr_2Ir_2O_7$.

I. INTRODUCTION

The realization of exotic ground states in pyrochlore iridates $A_2Ir_2O_7$ ($A =$ lanthanide element) culminating from the interplay among the crystal field effect, magnetic exchange interaction, and spin-orbit coupling (SOC) has generated significant interest in the contemporary condensed matter research. The Ir $5d$ electrons offer possibilities to explore the correlation effects in SOC-rich compounds. This has led to many recent theories predicting Weyl semimetals (WSM), topological insulators, axion insulators, Mott insulators, and Luttinger-Abrikosov-Beneslavskii non-Fermi liquids (NFL) [1–5]. Experimental verification of these predictions is still ongoing. The SOC-dominant Dzyaloshinskii-Moriya (DM) interaction causes these materials to undergo a finite temperature metal-insulator transition (MIT) coinciding with an "all in-all out" (AIAO) antiferromagnetically ordered ground state [6–11]. The ionic radius boundary for the MIT lies between Nd and Pr, $Pr_2Ir_2O_7$ being the sole compound in the iridate pyrochlore family, which is a paramagnetic metal. Despite the presence of magnetic interactions (Pr^{3+} is $J = 4$ and Ir^{4+} with $J_{eff} = 1/2$), $Pr_2Ir_2O_7$ does not show magnetic order and remains metallic down to the lowest measured temperature (0.3 mK), suggested to be a chiral metallic spin liquid [12,13]. This system is further intriguing since it exhibits spontaneous zero field Hall effect and logarithmic non-Fermi-liquid (NFL) behavior of magnetic susceptibility without spontaneous magnetization [14,15]. By having the doubly degenerate quadratically dispersed valence and conduction bands touching at the Γ point of the Fermi level,

it is known to have the Luttinger-semimetal (LSM) state [2,16,17]. This band touching is a 3D analog of bilayer graphene [18] and is also reported in a few other materials, including α-Sn and HgTe [19–22]. Due to the increased density of state (DOS) close to the fermi node, these materials have stronger electronic correlations than the linear-band crossing systems (Weyl and Dirac semimetals). This is supported by photoemission spectroscopy giving the effective band mass of electrons (6.3 m_0) in $Pr_2Ir_2O_7$ to be 300 times larger than in α-Sn [16,19]. It has been suggested [2,16] that long-range Coulomb interactions can transform the quadratic nodal semimetal $Pr_2Ir_2O_7$ into an NFL state, which can be further tuned by strain to other topological phases, such as a topological insulator or a WSM state, by breaking the inversion or time-reversal symmetry (TRS). Similar physics can be witnessed in the iridium phase diagram, where the LSM state in $Pr_2Ir_2O_7$ gives way to the WSM states in magnetic $Eu_2Ir_2O_7$ and $Sm_2Ir_2O_7$ [3,4,23]. Recent transport studies on Bi-doped Eu and Sm pyrochlore iridates have shown signatures of this WSM state up to 2% Bi substitution at Sm (3.5% in case of Eu) site, which goes over to a QBT state with further Bi doping [24,25]. Quantitatively, Bi doping tunes spin ordering and electronic bandwidth, leading to the melting away of the WSM phase into the QBT state, as is also the case when going from Eu and Sm iridates to $Pr_2Ir_2O_7$ in the phase diagram. In terms of phonon anomalies, our recent Raman studies investigated these topological phases as a function of Bismuth doping [26,27]. Previous studies of phonons in other pyrochlore iridates have also shown anomalous temperature dependence of phonons, associated with phonon-phonon, electron-phonon, and spin-phonon interactions as well as disorder-induced phase transitions [28–32].

*asood@iisc.ac.in

A single Fermi node shielded by time reversal and inversion symmetry as a result of strong electronic correlations and spin-orbit coupling (SOC) is of considerable interest [16]. With this in view, we explore in-depth temperature-dependent carrier dynamics and phonon excitations in $Pr_2Ir_2O_7$ using Raman spectroscopy. Raman scattering is a powerful tool for understanding the interaction between magnetic, electronic, and lattice degrees of freedom. It is effective to identify unique crystal field bands and mode splitting (if any) with better resolution (<0.15 meV) than resonant inelastic x-ray scattering (RIXS) or neutron diffraction experiments ($\sim$1 meV). In a recent study, the Raman phonon spectra of two materials, $Pr_2Zr_2O_7$ and $Pr_2Ir_2O_7$, with similar crystal structures but different electrical characteristics, were compared, which has shown evidence of electron-phonon coupling in semimetallic $Pr_2Ir_2O_7$ [33]. Additionally, it has been shown that both compounds have well-resolved crystal field excitations that couple strongly to phonons. While the temperature-dependent Raman spectra are reported, it is still unclear if QBT is the fundamental mechanism underlying electron-phonon coupling in $Pr_2Ir_2O_7$. In a recent terahertz experiment [17], $Pr_2Ir_2O_7$ demonstrated a significant dielectric constant at low temperatures, indicating strong electron-electron interactions in the QBT state. Raman scattering can reveal distinct signatures of these interactions as it is sensitive to charge density fluctuations. In this regard, our current research concentrates predominantly on the low-temperature Raman spectra of $Pr_2Ir_2O_7$ by carefully investigating the fingerprints of QBT. Apart from temperature-dependent phonon anomalies, we observe significant electronic Raman scattering (ERS) below a characteristic temperature T_Q which has been attributed to enhanced electron-electron interactions in the QBT state. This temperature scale T_Q is attributed to a crossover into the QBT state with non-Fermi-liquid-like behavior. In addition to this, the E_g phonon displays enhanced Fano resonance and anomalous linewidth broadening in the QBT state, indicating the strongest electron-phonon coupling strength for this mode. The electron-phonon interaction also has an impact on other phonons as exemplified in their anomalous frequency softening below T_Q. By using a qualitative model to fit the real part of the phono self-energy, we have attempted to quantify the relative strength of the phonon-phonon and electron-phonon interactions. Similar to a previous report [33], we also detected a crystal field excitation (CFE) at $\sim$460 cm^{-1}, associated with the transition from the ground state to the second excited state. Due to the coupling between this excitation and a T_{2g} phonon, this mode exhibits an anomalous softening of the frequency with decreasing temperature.

II. EXPERIMENTAL DETAILS

High-quality polycrystalline samples of $Pr_2Ir_2O_7$ were prepared via the standard solid-state reaction method using high-purity (>99.9%) precursors of Pr_6O_{11} and IrO_2. The phase purity of synsized samples was checked using the Bruker D8 advance powder x-ray diffractometer. Magnetic susceptibility and resistivity measurements were performed using a Physical Property Measurements System (Quantum Design). The elemental composition of the sample was determined using energy dispersive x-ray spectroscopy (EDS)

analysis. The oxidation states of the elements were characterized by x-ray photoelectron spectroscopy (XPS) using a thermo scietific K-ALPHA, Surface analysis system equipped with a monochromatic Al source ($K_\alpha = 1486.6$ eV). The unpolarized Raman spectrum was recorded in backscattering geometry using a HORIBA LabRAM HR Evolution spectrometer and Peltier-cooled CCD (Jobin Yvon, Syncerity). The excitation wavelength was 532 nm and the laser power was minimized to <0.3 mW to avoid any local heating of the sample. The low-temperature Raman measurements (5 to 295 K) were performed using closed-cycle He-cryostat, Cryostation S50, Montana.

III. RESULTS AND DISCUSSIONS

$Pr_2Ir_2O_7$, or more accurately $Pr_2Ir_2O_6O'$, is an iridate from the pyrochlore family that crystallizes in the cubic space group $Fd\bar{3}m$ (z = 8) with Pr^{3+} at Wyckoff position 16d (0.5,0.5,0.5), Ir^{4+} at 16c (0,0,0), O and O' at 48f (x,0.125,0.125), and 8b (0.375,0.375,0.375), respectively. Both Pr and Ir form interpenetrating corner-shared tetrahedral networks running parallel to the body diagonals of the cubic unit cell. While the Ir ion is coordinated with six O ions to form an IrO_6 octahedron, Pr is in an eightfold environment, surrounded by six O and two O' ions [34]. The crystal structure of our sample was verified using x-ray diffraction (XRD), as shown in Fig. 1(a). The observed powder-XRD pattern could be satisfactorily fitted using the cubic pyrochlore structure (space group $Fd\bar{3}m$, z = 8) with no extra peaks. The good quality of the refinement can be inferred from the fitted and the difference plots in the figure ($\chi^2 = 4.6$ and the extracted lattice parameter = 10.41 Å). Based on the refinement results, the presence of antisite disorder or off-stoichiometry in our samples can be ruled out within the error bars of this technique.

The transport characteristics and magnetization were studied at low temperatures, confirming metallic behavior and the absence of any long-range magnetic order down to the lowest recorded temperature (2 K) [see Figs. 1(b) and 1(c)], which is in agreement with the previous reports [12,13,17]. The resistivity in $Pr_2Ir_2O_7$ decreases with decreasing temperature and flattens below 50 K, earlier proposed to be due to the Kondo effect [33], however, it was later attributed to the interplay between a decreasing scattering rate and a decreasing charge density upon cooling, as expected in a 3D-LSM by Cheng et al. [17]. The modified Curie-Weiss law, i.e., $\chi = \chi_0 + \frac{C}{T-\theta_{CW}}$ is used in the inset of Fig. 1(c) to fit the $\chi(T)$ data in the high-temperature range between 150 and 295 K. A reasonably good fit of $(\chi - \chi_0)^{-1}$ vs T implies that the paramagnetic state obeys modified Curie-Weiss behavior. The fit yields $\chi_0 = 2.64 \times 10^{-3}$ emu/mole, the effective moment $\mu_{eff} = 3.89 \mu_B$ and Curie-Weiss temperature $\theta_{CW} = -18.76$ K in agreement with previously reported values [13,35–37]. The finite value of θ_{CW} arises due to Ir-5d electron mediated antiferromagnetic type Ruderman–Kittel–Kasuya–Yosida (RKKY) interactions among Pr-4f atoms.

The elementary composition of the sample was determined using energy dispersive x-ray spectroscopy (EDS) and scanning electron microscopy (SEM) data collected on fine powder of $Pr_2Ir_2O_7$. The observed EDS spectra indicated only the expected Pr and Ir signals present in the EDS (atomic
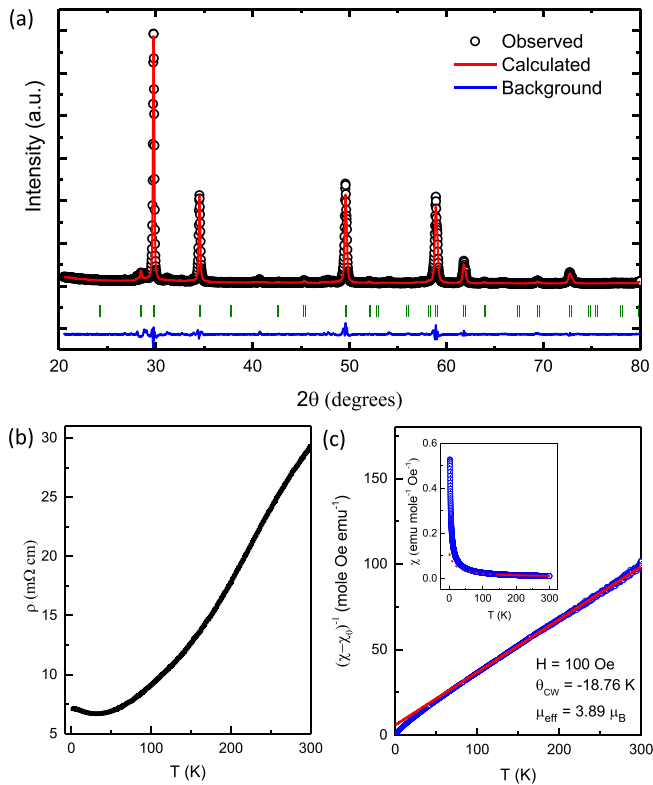
FIG. 1. (a) Powder x-ray diffraction pattern of $Pr_2Ir_2O_7$. The vertical green bars below the diffraction pattern indicate the positions of the Bragg peaks of the pyrochlore phase. The fitted profile and difference plot is shown using red and blue color, respectively. [(b) and (c)] Temperature dependence of resistivity (ρ) and inverse magnetic susceptibility, respectively for the $Pr_2Ir_2O_7$ sample. The inset in (c) shows the measured magnetic susceptibility as a function of temperature. Solid red lines in both the main graph and inset indicate fit to the Curie-Weiss law and the dashed line in the inset is the extrapolated fit up to zero Kelvin.

percentages given, Pr-18.72%, Ir-17.57%) (see Fig. S1 in Ref. [38]). The Pr/Ir ratio which is important to maintain the oxygen content in $Pr_2Ir_2O_7$ is found to be consistent with the stoichiometric ratio of Pr/Ir (1:1), when measured at different locations of the samples with a number of iterations (4).

Further, the oxidation state of the cations in $Pr_2Ir_2O_7$, specifically for the iridium ion which largely governs the electronic and magnetic properties of these materials were investigated using x-ray photoemission spectroscopy (XPS) measurements (see Fig. S2 [38]). The measured XPS spectra were calibrated using the carbon $1s$ peak with binding energy (BE) at 284.8 eV. The core-level spectra for Ir-$4f$ and Pr-$3d$ have been analyzed in detail using standard CASAXPS software package, as shown in Figs. S2(a) and S2(b) [38]. The background is defined using the Shirley function, while fitting the Pr-$3d$ and both the lower and higher BE spin-orbit doublets (doublet II and doublet I, respectively) for Ir-$4f$ spectra. Deconvolution of the spectrum was performed using the Gaussian-Lorentz (GL) peak profile function. The photoemission spectra of Ir based compounds is characterized by pair of spin-orbit split doublets (I and II) [39,40]. This in some cases has been attributed to the presence of higher oxidation

states of Ir in previous XPS studies [35,41]. However, HAX-PES study on iridium oxide (IrO_2) by Kahk *et al.* [42] and an analytical model by Kotani *et al.* [43] have identified it as screened (II) and unscreened doublets (I) of Ir-core level. The intensity of the screened doublet is proportional to the sample's electrical conductivity. The double II peak is expected to be dominant in metallic samples (as is the case in $Pr_2Ir_2O_7$), but is weaker or absent in insulating materials, such as the Mott insulating iridate $Y_2Ru_2O_7$ [44]. The binding energies from the fitting for the narrow and intense doublet II in this case are found to be 65.5 and 62.4 eV respectively for $4f_{7/2}$ and $4f_{5/2}$ states. The spin-orbit splitting between $4f_{5/2}$ and $4f_{7/2}$ is found to be to be 3 eV, which is in good agreement with the reported values [35,40,41,45]. The XPS peaks of Pr-$3d$ spectra consist of spin-orbit splitted doublets of $3d_{5/2}$ and $3d_{3/2}$. The peak deconvolution of Pr-$3d$ XPS spectra showed two main peaks, two satellite peaks, s and s', and an extra peak marked t'. All these peaks are characteristics of the Pr^{3+} ions [46]. The s and s' satellite structures origin from strong mixing of the two final states of $3d^94f^2$ and $3d^94f^3$, while the t' structure was caused by the multiplet effect. Our XPS analysis showed that both the cations (Pr^{3+} and Ir^{4+}) have nominal valence states which rules out oxygen-off stoichiometry in our sample.

The factor group analysis on the $Fd\bar{3}m$ space group of the unit cell gives six Raman active modes ($A_{1g} + E_g + 4T_{2g}$) in $Pr_2Ir_2O_7$. The observed vibrations involve O and O' atoms since the Pr and Ir sites have center of symmetry [28]. Temperature-dependent Raman spectra of $Pr_2Ir_2O_7$ between 5 to 295 K are shown in Fig. 2. The observed phonon modes are assigned as follows: Ir-O-Ir bending modes E_g (~ 350 cm^{-1}) and A_{1g} (~ 504 cm^{-1}); T_{2g}^4 (~ 648 cm^{-1}) as Ir-O stretching mode; T_{2g}^2 (~ 460 cm^{-1}) and T_{2g}^1 (~ 296 cm^{-1}) as Pr-O stretching, and T_{2g}^3 (~ 550 cm^{-1}) involving vibration of O' surrounded by eight Pr ions [28]. Based on earlier neutron scattering study [47], an additional mode near 460 cm^{-1} at low temperatures is ascribed to Pr-crystal field excitation [33]. The peak positions, and intensities of most of the phonons and CFE observed here agree qualitatively with the previous Raman spectroscopy measurements [33]. The A_{1g} mode intensity is stronger in XX polarization in the previous report as compared to unpolarized spectra in the current study as expected due to its symmetry. The previously reported interband electronic transition mode at 250 cm^{-1} is not seen, and the strong peak at 650 cm^{-1} appears as a weak shoulder peak to T_{2g}^4 mode in this report. The weak modes observed beyond T_{2g}^4 have been identified as second-order Raman modes [48,49]. Raman spectrum at 5 K in the spectral region of 70 to 1700 cm^{-1} is shown in Fig. 3(a). Most notable is a flat continuum (marked by a shaded portion) up to the highest measured frequency over which Raman modes are superimposed, a feature that was not reported in the previous study on single crystal of $Pr_2Ir_2O_7$ [33]. Figure S3(a) [38] shows the standard silicon spectra at 295 K as a reference, confirming that the signal spectral response over the measured spectral range does not contain any artificial slope. This demonstrates that the observed continuum is inherent to the sample. Our analysis, discussed in the next section, assigns this continuum to electronic Raman scattering (ERS) from Ir^{4+} itinerant electrons.
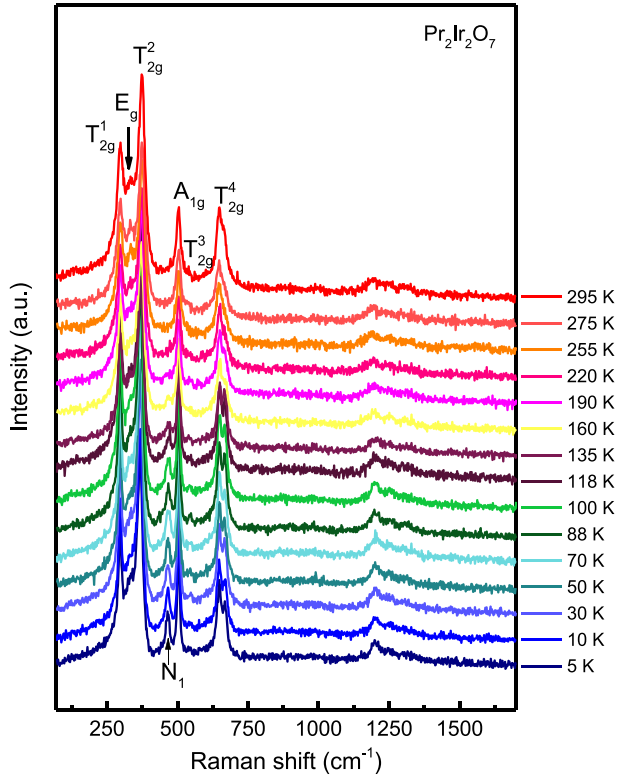
FIG. 2. Temperature dependent Raman spectra of $Pr_2Ir_2O_7$; upward vertical arrow indicates evolution of crystal field excitation N_1.

A. Electronic Raman scattering

Before discussing the origin of the broad continuum in Raman spectra, it may be pertinent to recall a recent terahertz experiment on films of $Pr_2Ir_2O_7$, which shows a large dielectric constant at low temperatures, suggesting electron-electron interactions to be ~100 times larger than the kinetic energy [17]. In a 3D system with the QBT (LSM), the long-range Coulomb interaction may stabilize a quantum critical NFL ground state (protected by cubic and time reversal symmetry) [2,50]. Such an unconventional zero temperature phase would exhibit distinctive nontrivial power laws in temperature or frequency of different response functions of the system [2]. The LSM state is also anticipated to have stronger electronic correlations than the linear band-crossing systems because of the sharply rising density of states (DOS) towards the edge of the band contacting point [16,17]. In this situation, ERS can be a reliable alternative method for supplementing transport and optical studies.

The observed continuum shown in Fig. 3(a) is temperature dependent. A direct comparison is shown in Fig. S3(b) [38] between observed spectra at 5 and 295 K, which clearly shows the spectral weight decrease in 295 K data in comparison to 5 K data towards high frequency sides. Such a flat continuum has been previously observed in Raman measurements of semimetallic $SrIrO_3$ [51], superconducting $YBa_2Cu_3O_7$ [52], $YBa_2Cu_3O_y$ [53,54], $Bi_2Sr_2(Ca_xY_{1-x})Cu_2O_8$ [53] and $Ba(Fe_{1-x}Co_x)_2As_2$ [55], as well as in optical conductivity measurements in URu_2Si [56], UPt_3 [57], Sr_2RuO_4 [58] and in an iridate of the same family $Nd_2Ir_2O_7$ [59]. This broad

spectrum is created when light is inelastically scattered by charge density fluctuations in superconductors and metals. Here, we analyze our results based on a memory function-based model [51,53,55,57,58,60,61] to quantify the dynamic scattering $\Gamma_s(\omega, T)$. The memory function is expressed as $M(\omega, \mathrm{T}) = \hbar\omega\lambda(\omega, T) + i\Gamma_s(\omega, T)$, where $\Gamma(\omega)$ and $\lambda(\omega)$ related by the Kramers-Kronig transformation represent the relaxation rate and mass enhancement factor, respectively. In terms of memory function $M(\omega)$, the complex Raman response function $\chi(\omega)$ is given by [51,53,57,60],

$$\chi(\omega, T) = \frac{M(\omega, T)}{\hbar\omega + M(\omega, T)} \quad (1)$$

The Raman intensity $I_{ERS}(\omega)$ is related to the imaginary part of $\chi(\omega, \mathrm{T})$, given as

$$I_{ERS}(\omega) = Q\chi_e''(\omega, T), \quad (2)$$

where

$$\chi_e''(\omega, T) = \frac{\hbar\omega\Gamma_s(\omega, T)}{[\hbar\omega(1 + \lambda(\omega, T))]^2 + [\Gamma_s(\omega, T)]^2}. \quad (3)$$

The dynamical scattering rate $\Gamma_s(\omega, T)$ has the general form

$$\Gamma_s(\omega, T) = \left[\Gamma_{s0} + \frac{[\beta^2K^2T^2 + \hbar^2\omega^2]^e}{(\hbar\omega_c)^{2e-1}}\right]\Phi\left(\frac{\omega}{\omega_c}\right), \quad (4)$$

where e is the critical exponent characterizing Fermi-liquid ($e = 1$) or non-Fermi-liquid ($e \neq 1$)) behavior, Γ_{s0} is the temperature-independent relaxation rate, β is a coefficient determining the relative strength of elastic and inelastic scattering processes (optimal value to produce the best fit $\beta = \pi$) and $\phi(\frac{\omega}{\omega_c}) = \frac{1}{1+(\frac{\omega}{\omega_c})^2}$ is a cutoff function. The bandwidth determines the cut-off frequency, which in present case is 0.4 eV for iridates. The parameter Q in Eq. (2) is a fitting parameter representing the strength of the ERS. The scattering rate proportional to T^2 and a component proportional to ω^2 are characteristics of a Fermi liquid [$e = 1$ in Eq. (4)] [56]. However, when two quadratically dispersed low energy bands meet at a single point in a Brillouin zone, it is known that the system will show instabilities toward a nematic state driven by the Coulomb interactions [62]. In such situations, the typical Fermi-liquid state breaks down, with the critical exponent $e \neq 1$. Fitting the broad continuum in our Raman data using Eqs. (2)–(4) gives $e = 0.65$, showing NFL state in $Pr_2Ir_2O_7$. Figure S4 [38] shows how Fermi-liquid model, with $e = 1$, overestimates the spectrum towards high frequencies, whereas the Marginal Fermi-liquid model with $e = 1/2$ overestimates the spectrum towards low frequencies and the best fit has been found for $e = 0.65$ (non-Fermi liquid). The observed continuum is present at all temperatures in our experiments (see Fig. S5 [38]). It should be noted that, unlike $Nd_2Ir_2O_7$ [59], where the critical exponent of the scattering rate varied with temperature, $Pr_2Ir_2O_7$ has a constant value of e across all recorded temperatures with a temperature dependent scaling parameter (Q). For better understanding of the nature of the electronic continuum, we have plotted the I_{ERS} obtained from the fitting of the Raman spectra on an enlarged scale in Fig. 3(b) and the graph clearly shows that following a linear rise at low frequencies, the continuum peaks between 100 to 200 cm^{-1}, depending on the temperature and then has a
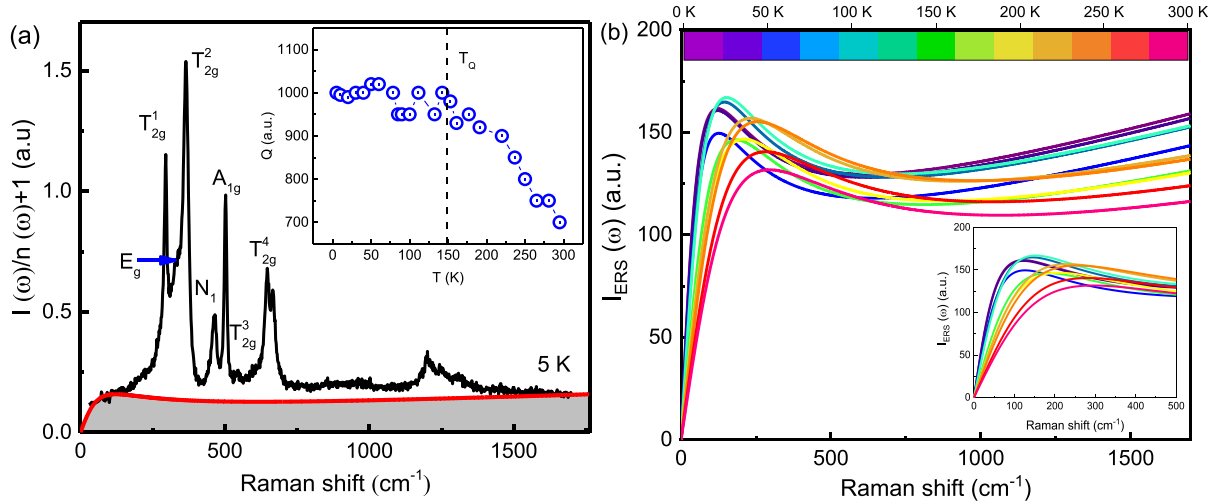
FIG. 3. (a) 5 K Raman spectra of $Pr_2Ir_2O_7$; shaded region indicates flat electronic continuum; red curve shows the fit to the NFL memory function formalism; inset shows the temperature dependence of the scaling factor Q of the NFL model; vertical black dashed line indicate the temperature scale of QBT denoted by T_Q (b) Extracted I_{ERS} of the electronic continuum from fitting the Raman spectra with memory function formalism at various measured temperatures; inset shows the low frequency region of the electronic continuum on an enlarged scale.

modest increase with Raman shift. The intensity of the observed ERS is nearly constant at low temperatures and beyond a characteristic temperature T_Q ($\sim$150 K), its amplitude [defined by the prefactor Q in Eq. (2)] exhibits a decline [inset of Fig. 3(a)]. Interestingly, strongly correlated quasi-particle-like features are seen in a recent ARPES measurement on single crystals of $Pr_2Ir_2O_7$ [17], which are enhanced below 100 K and have characteristics consistent with the NFL behavior. In this situation, our findings provide an alternate identification of the NFL state with the developing QBT state at low-temperatures in 3D-LSM $Pr_2Ir_2O_7$.

Additionally, to confirm that the feature is not arising due to the crystallinity of the sample, we have conducted a comprehensive characterization of our sample, and our findings reveal that the sample exhibits single pyrochlore phase with a high degree of crystallinity and minimal structural defects or grain boundaries (see Fig. 1 and Figs. S1 and S2 [38]). Further, if the continuum was arising due to the polycrystalline nature of the sample, then it should not show a strong temperature dependent behavior along with a characteristic temperature scale. This analysis indicates that the continuum is intrinsic to the sample as a signature of the evolving band topology and strong electron-electron interaction in the QBT state.

B. Temperature dependence of CFE and phonons

We now turn to the temperature evolution of the crystal field and phonon excitations. The CF and all the T_{2g} and A_{1g} modes are well-fitted by a symmetric Lorentzian line shape (see Fig. 4). In contrast, the E_g mode fits best using asymmetry line shape given by the Breit-Wigner-Fano (BWF) function written as

$$I(\omega) = I_0 \frac{1 + \left(\frac{\omega - \omega_0}{q\Gamma}\right)^2}{1 + \left(\frac{\omega - \omega_0}{\Gamma}\right)^2}, \quad (5)$$

where q is the Fano asymmetry parameter. For $1/q = 0$, the line shape becomes Lorentzian, representing the bare phonon spectrum.

C. Temperature tunable Fano resonance

The Fano resonance arises from the interference between the Raman amplitudes of an electronic continuum and a discrete phonon excitation [63]. Similar asymmetric line shapes
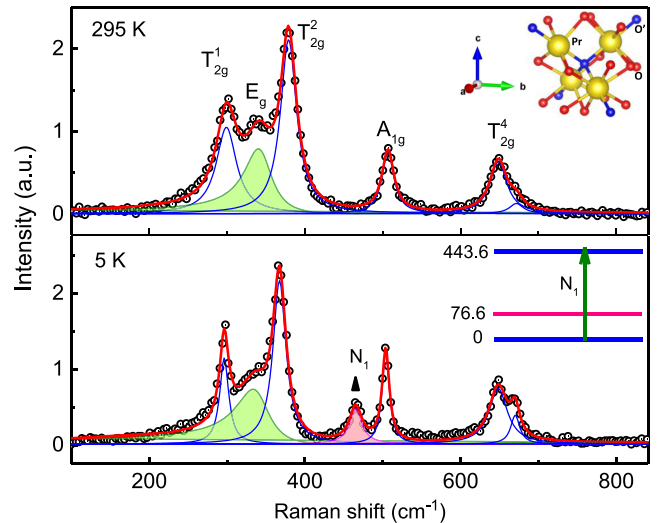

FIG. 4. The cumulative fit to the observed phonon and crystal field modes (E_g with BWF function and rest of the five modes with Lorentzian), top and bottom panels show 295 and 5 K, respectively. The green and magenta shaded regions indicate the E_g and CFE modes, respectively (the background has been subtracted while fitting the phonons). The top inset shows the Pr ion environment surrounded by eight oxygen ions in the pyrochlore structure, and the bottom inset depicts the observed crystal field transition (energy levels shown are in cm^{-1}) of the Pr^{3+}.
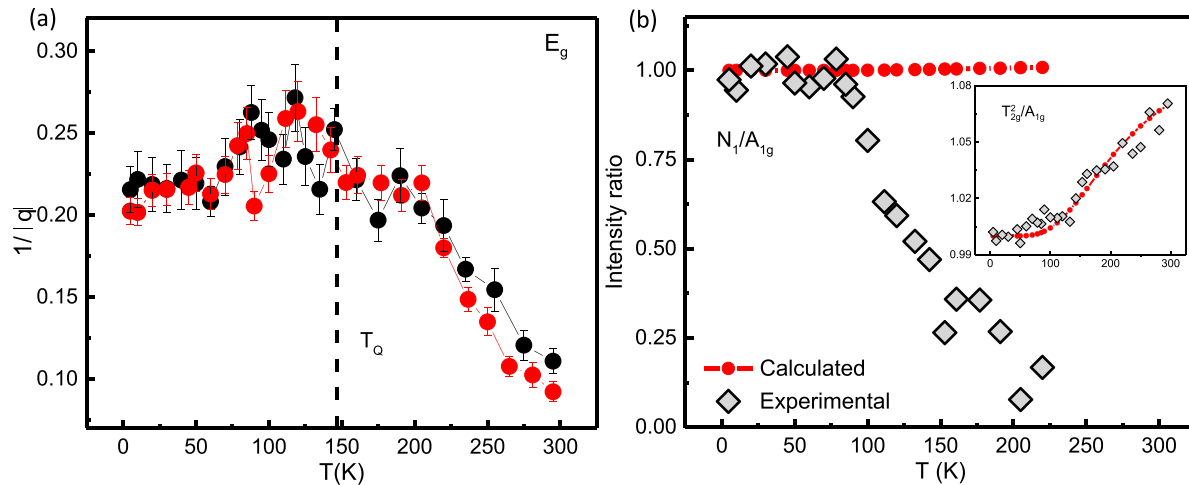
FIG. 5. (a) 5 K Raman spectra of $Pr_2Ir_2O_7$; shaded region indicates flat electronic continuum; red curve shows the fit to the NFL memory function formalism; inset shows the temperature dependence of the scaling factor Q of the NFL model; vertical black dashed line indicate the temperature scale of QBT denoted by T_Q (b) The cumulative fit to the observed phonon and crystal field modes (E_g with BWF function and rest of the five modes with Lorentzian), top and bottom panels show 295 and 5 K, respectively. The green and magenta shaded regions indicate the E_g and CFE modes, respectively (the background has been subtracted while fitting the phonons). The top inset shows the Pr ion environment surrounded by eight oxygen ions in the pyrochlore structure, and the bottom inset depicts the observed crystal field transition (energy levels shown are in cm^{-1}) of the Pr^{3+}.

for the E_g mode have been observed in other pyrochlore iridate such as $Eu_2Ir_2O_7$ and attributed to presence of strong EPC [26,28]. The Breit-Wigner-Fano fits to the E_g phonon for $Pr_2Ir_2O_7$ at various temperatures are shown in Fig. S6(a) [38]. The fitting shows that the Fano asymmetry manifests itself by spectral weight gain on the low-frequency side at the cost of spectral weight loss on the high-frequency side. At all temperatures, the E_g mode is well-fitted with the Fano profile and the extracted asymmetry parameter $1/|q|$, shown in Fig. 5(a) is practically constant up to T_Q and decreases as the temperature increases. The asymmetry parameter $1/|q|$ is a measure of the coupling strength between the phonon and charge degree of freedom [28,64]. The decline of $1/|q|$ value above T_Q implies enhanced coupling of the E_g phonon with the electronic continuum at low temperatures, arising due to large electronic DOS close to the Fermi node due to the QBT [65]. The temperature dependence of the E_g phonon, in terms of Fano asymmetry in this case allows us to extract the electron-phonon coupling strength for this mode.

D. Origin of the crystal field excitation

The CFE is marked as N_1 in Fig. 2. As the spin-orbit coupling energy in pyrochlore iridate is typically larger than the crystal field splitting for the f electrons, the latter is regarded as a perturbation. As a result, the D_{3d} crystal electric field splits the Pr^{3+} $^3H_4$ levels of $4f$ atomic orbital bearing a orbital angular momentum ($J = 4$) into nine multiplets ($2A_{1g} + A_{2g} + 3E_g$) in the $Pr_2Ir_2O_7$ crystal [66]. The ground state (GS) is defined by the E_g non-Kramers doublet. The second and fourth excited states are doublets at 443.6 and 766.2 cm^{-1}, respectively, whereas the other three excited levels—76.6, 661.4, and 887.2 cm^{-1}—belong to singlet states [66–68]. Experimental evidence has been provided by inelastic neutron scattering measurements, showing five peaks due to CFE [47].

For $Pr_2Ir_2O_7$, we detect one Raman band at 460 cm^{-1} at 5 K, which is substantially below the threshold for thermally filling excited crystal-field states. Therefore all CEF excitations at this temperature originate from the ground state. The observed band thus corresponds to the transition from the ground state to the second excited state of the $^3H_4$ manifold of the Pr^{3+} ion with an energy difference of 443.6 cm^{-1} (Fig. 4). The integrated intensities of the N_1 and T_{2g}^2 modes with respect to the strong and well-resolved A_{1g} mode are shown in Fig. 5(b). It can be seen in the inset that the relative intensity of the T_{2g}^2 mode rises with temperature, as expected by the Bose population factor, i.e., $(n(\omega_{T_{2g}^2}) + 1)/(n(\omega_{A_{1g}}) + 1)$. On the other hand, the intensity of the N_1 mode deviates from the phonon population factor and exhibits an opposite pattern, confirming the origin of this excitation to be nonphononic. The temperature evolution showing strong suppression of this mode at higher temperatures (above 200 K) is shown in Fig. S6(b) [38]. The CFEs are mostly observed at low temperatures since they have a considerable linewidth broadening at higher temperatures [69]. The large broadening of the crystal-field levels with increasing temperature is caused by the electron-phonon interaction from two primary sources. One is the nonradiative decay between crystal-field levels within a single multiplet with acoustic phonon emission and absorption and the second one is the transition between crystal field levels caused by the inelastic scattering of phonons [70–72].

E. Phonon renormalization in terms of self-energies

We now focus on the temperature dependence of phonon frequencies and linewidths shown in Figs. 6(a) and 6(b), respectively. To bring out the anomalous temperature dependence, we use a simple cubic anharmonic model of phonon self-energies, which involves the decay of an optical phonon into two phonons of equal frequencies $\omega_0/2$ [73]. This
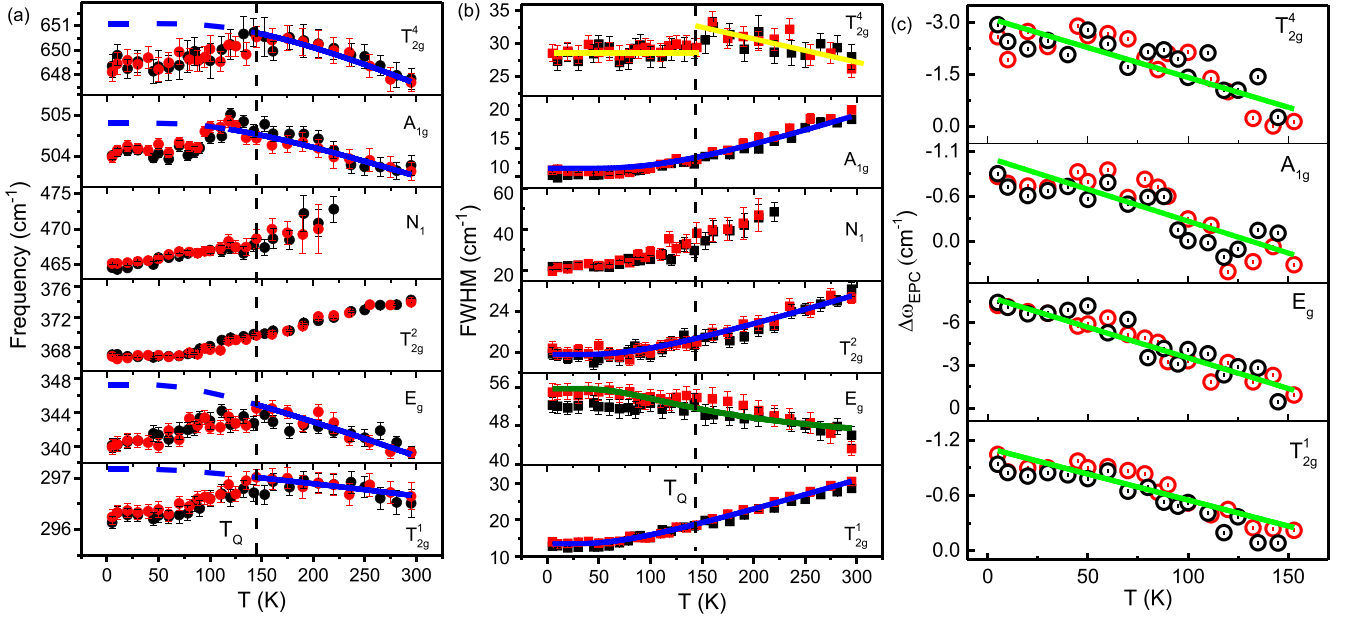
FIG. 6. [(a) and (b)] Temperature variation of phonon frequencies and linewidths, respectively; two different color symbols indicate data from two independent sets of measurements; vertical black dashed line indicates the temperature scale of QBT denoted by T_Q. Solid blue lines are fit to the anharmonic model (fitted to the combined set of data from both sets of measurements) and extended to zero Kelvin by dashed lines. Dark green line (in (b)) are fit to Eq. (7), whereas the yellow lines are guide to the eye. (c) The anharmonic corrected $\Delta\omega_{EPC}$ below T_Q for different phonon modes. Solid green lines are fit to Eq. (8).

predicts

$$\omega_{\text{anh}}(T) = \omega_0 + CG(\omega, T),$$
$$\Gamma_{\text{anh}}(T) = \Gamma_0 + DG(\omega, T), \tag{6}$$

where $G(\omega, \text{T}) = [1 + 2n(\omega_0/2)]$. The parameters C (<0) and D (>0) represent phonon-phonon interaction strength. The solid blue lines in Figs. 6(a) and 6(b) are the fit to the cubic anharmonic model above T_Q, extrapolated by dotted lines to lower temperature (values of C and D are given in Table I in Ref. [38]). It can be seen that all the phonon modes deviate from the anharmonic model prediction and show anomalous behavior below T_Q. The anomalous frequency softening below T_Q is larger for the E_g and T_{2g}^4 modes ($\sim$4 and 3 cm^{-1}, respectively), as compared to the A_{1g} and T_{2g}^1 modes, ($\sim$1 cm^{-1}). Interestingly, the T_{2g}^2 phonon exhibits anomalous frequency softening by a large amount ($\sim$8 cm^{-1}) over the entire temperature range. We note that, in contrast to the earlier work [33], our experiments clearly show a large anomalous linewidth broadening ($\sim$12 cm^{-1}) of the E_g phonon with decreasing temperature. This demonstrates that at low temperatures, electron-phonon interaction for the E_g phonon has a substantial temperature dependence that can only be partly offset by $\Gamma_{\text{ph-ph}}$ [see Fig. 6(b)]. The following equation has been used to fit to the linewidth of the E_g mode in Fig. 6(b), which depicts the decay of an optical phonon into an electron-hole pair [65,74,75],

$$\Gamma_{\text{el-ph}}(T) = \Gamma_0 + F\left(n_f\left(\frac{-\hbar\omega_0}{2}, T\right) - n_f\left(\frac{\hbar\omega_0}{2}, T\right)\right), \tag{7}$$

where $n_f = \frac{1}{1+e^{\frac{\hbar\omega_0}{KT}}}$ is the Fermi-Dirac distribution function at temperature T, Γ_0 is the bare phonon linewidth and F is an overall fitting parameter which should be proportional to the mode coupling strength, and the available electronic density of states. The frequency ω_0 is the bare phonon frequency at zero temperature. The observed drop in linewidth with increasing temperature is caused by a decrease in the occupation of filled states below E_f while the occupancy of unoccupied states increases. The linewidths of all other phonons (A_{1g}, T_{2g}^1 and T_{2g}^2), is monotonic and regular, i.e., linewidth decreases with decreasing temperature. It is worth noting that even though the linewidths of, T_{2g}^1 and A_{1g} modes are not seen to be anomalous, they show large phonon-phonon interaction strength (large value of D, $\sim$10.9 cm^{-1} for A_{1g} and $\sim$9.3 cm^{-1} for T_{2g}^1 as compared to other modes) and change by a significant amount($\sim$16 and 10 cm^{-1}, respectively). The temperature influence on the T_{2g}^4 linewidth is small [see Fig. 6(b)]. The earlier study by Xu *et al.* [33] used an interband electron-phonon scattering model to explain the relationship between linewidth and temperature, however, the linewidth predicted by the adopted model increases with increasing temperature, which is contrary to the idea that band touching might be the cause of the EPC as interband scatterings are more pronounced at low temperatures [16,17]. In our study except for the E_g mode, the linewidths of other phonons can be explained by cubic anharmonic model [Eq. (6)] in the operating temperature range. The E_g mode which is anomalous throughout the measured temperature range is fitted by Eq. (7) that predicts higher linewidth at low temperatures. This supports the fact that origin of the EPC is attributed to the quadratic band touching at low temperatures. We further

continue to focus on the interesting part of the anomalous temperature dependence of all phonon frequencies which was not covered in the earlier work on $Pr_2Ir_2O_7$ [33].

Spin-phonon, electron-phonon, and phonon-phonon interaction are the three primary leading mechanisms contributing to the phonon self-energies. $Pr_2Ir_2O_7$ does not show long-range magnetic ordering, thus ruling out the contribution of the spin-phonon coupling. The phonon-phonon anharmonic interaction term has a modest influence and causes a monotonic change in frequency and linewidth with temperature. Therefore electron-phonon coupling (EPC) is the dominant mechanism behind the anomalous phonon renormalization in $Pr_2Ir_2O_7$. To quantify the effect of EPC we need a model to give temperature dependence of the real part of self-energy of a phonon $\Delta\omega_{EPC}(T)$ due to electron-phonon interaction. In absence of such a model in literature, we adopt a simple linear temperature dependence of $\Delta\omega_{EPC}(T)$:

$$\Delta\omega_{EPC}(T) = A(T - T_Q) \qquad (8)$$

where, $\Delta\omega_{EPC} = \omega_{anh} - \omega_{obs}$ and $T_Q = 150$ K ($A > 0$, represents the EPC strength). This expression for $\Delta\omega_{EPC}$ results in the anomalous softening of phonons below T_Q. Equation 8 gives satisfactory fits to the data for all phonons (except for the T_{2g}^2), as shown by solid green lines in Fig. 6(c). This demonstrates that the trend below $T < T_Q$ may be explained by our simplistic approximation of fitting the measured data by a linear fit of $A(T - T_Q)$.

From the extracted value of the fitting parameter A (shown in Table I in Ref. [38]), it is evident that the E_g mode is the one where the EPC is most visible. The observed Fano asymmetry and anomalous linewidth broadening with decreasing temperature are further evidence in favor of this. As the E_g mode directly involves Ir-O-Ir bending, the indirect electron hopping between the Ir ions contributes strongly to the electronic bandwidth and hence contributes to linewidth broadening at low temperatures and anomalous frequency softening below T_Q. The behavior of T_{2g}^2 mode is unique from other phonons and shows anomalous softening of frequency with decreasing temperature over the entire measured range of temperature.

Interestingly, the temperature behavior of the CFE N_1 also follows the same trend as the T_{2g}^2 mode. The CFE frequency is likely to harden with lowering temperature as the lattice contracts upon cooling [26,32,76]. Contrary to this, a softening of the CF line is seen across the whole temperature range, similar to the case in $Pr_2Zr_2O_7$ [69]. This peculiar behavior cannot be accounted for by either a pure CFE or a pure phonon excitation. In the case of rare-earth ions, the CF levels are modulated by phonons to form vibronic bound states due to the overlapping energy scales of these excitations [69,77–79]. The vibronic coupling is induced by the modification of the electron-cloud distribution of the CF states by the lattice vibrations. Such a coupling can happen when two elementary excitations with the same symmetry mix with one another. Depending on the coupling strength, the quasiparticles can renormalize their frequencies and linewidths [78]. From the perturbation theory, the effects of renormalization are maximum when the energy difference between the pristine excitations is small. In $Pr_2Ir_2O_7$, the nonsplit CF doublet (see inset of Fig. 4) and the T_{2g}^2 phonons (Pr-O) stretching are close

in energy and therefore the vibronic coupling is strong (see Fig. 6). Similar vibronic interaction between a crystal field doublet (E_g) and a T_{2g} phonon has been observed for $Pr_2Zr_2O_7$ [69] in a recent temperature dependent Raman study. As the Pr^{3+} ions' closest neighbors are the plane of oxygen atoms, it is most likely that phonons involving planar oxygen atoms modifies the crystal field. The vibronic coupling with the CFE will also cause the considerable renormalization of the T_{2g}^2 mode, leading to temperature behavior significantly different from the expected lattice anharmonicity or the EPC.

F. Role of QBT in EPC

The temperature dependence of the Fano asymmetry parameter, as well as the fact that phonon renormalization is more prominent at low temperatures (below T_Q), both point to the role of QBT's in the development of the EPC. $Pr_2Ir_2O_7$ hosts an isolated Fermi node at Γ point of the Brillouin zone by touching of two doubly degenerate quadratically dispersed valence and conduction bands. According to the recent ARPES spectra, the bands disperse further towards higher binding energies with a narrow gap ($\leqslant$40 meV) prolonged along the Γ-L cut all the way to the W point without crossing E_f [16,80]. This energy gap, which falls within the range of phonon frequencies, would provide an appropriate phase space for interband phonon-electron scattering [33]. The anomalously high, low temperature dielectric constant discovered in recent terahertz measurements, as well as the fact that quasi-particle-like characteristics were identified in ARPES data only at low temperatures [16,17], support our conclusion that the enhanced EPC at low temperatures is driven by the band touching due to the rapidly increasing electronic density of states near E_f. The transition probabilities for the phonon-assisted interband transitions at the phonons' energy (ω_{ph}) increase at low temperatures (below T_Q). As the temperature rises, more and more charge carriers are thermally excited above E_f, causing Pauli blocking of low-energy interband transitions around the touching point of the valence and conduction bands and thus weakening the EPC at high temperatures [74]. Overall, the temperature dependence of the Fano asymmetry parameter, the scaling factor of ERS as well as the distinct phonon anomalies allows us to identify the scaling temperature of QBT which was not identified in prior investigations.

In summary, we investigated the temperature dependence of phonons and crystal field excitations of $Pr_2Ir_2O_7$ from 5 to 295 K. The crossover into the QBT state results in the unusual softening of all the phonons below T_Q. The Ir-O-Ir bending E_g phonon is most impacted by EPC. Our results, based on the qualitative analysis of the electronic Raman scattering, point to a novel NFL-like scattering rate in this correlated robust SOC system, which is more evident in the low temperature QBT state. Below T_Q, both the ERS amplitude and the Fano asymmetry of the E_g phonon are enhanced, confirming strong electron-electron and electron-phonon interactions in the QBT state. Our findings may motivate further theoretical and experimental work into the microscopic mechanisms behind electron-phonon interactions in the QBT state.

[1] X.-P. Yao and G. Chen, $Pr_2Ir_2O_7$: When luttinger semimetal meets melko-hertog-gingras spin ice state, Phys. Rev. X **8**, 041039 (2018).

[2] E.-G. Moon, C. Xu, Y. B. Kim, and L. Balents, Non-fermi-liquid and topological states with strong spin-orbit coupling, Phys. Rev. Lett. **111**, 206401 (2013).

[3] W. Witczak-Krempa and Y. B. Kim, Topological and magnetic phases of interacting electrons in the pyrochlore iridates, Phys. Rev. B **85**, 045124 (2012).

[4] X. Wan, A. M. Turner, A. Vishwanath, and S. Y. Savrasov, Topological semimetal and Fermi-arc surface states in the electronic structure of pyrochlore iridates, Phys. Rev. B **83**, 205101 (2011).

[5] L. Savary, E.-G. Moon, and L. Balents, New type of quantum criticality in the pyrochlore iridates, Phys. Rev. X **4**, 041027 (2014).

[6] C. Donnerer, M. C. Rahn, M. M. Sala, J. G. Vale, D. Pincini, J. Strempfer, M. Krisch, D. Prabhakaran, A. T. Boothroyd, and D. F. McMorrow, All-in–all-out magnetic order and propagating spin waves in $Sm_2Ir_2O_7$, Phys. Rev. Lett. **117**, 037201 (2016).

[7] K. Matsuhira, M. Wakeshima, R. Nakanishi, T. Yamada, A. Nakamura, W. Kawano, S. Takagi, and Y. Hinatsu, Metal–insulator transition in pyrochlore iridates $Ln_2Ir_2O_7$ (Ln = Nd, Sm, and Eu), J. Phys. Soc. Jpn. **76**, 043706 (2007).

[8] H. Zhang, K. Haule, and D. Vanderbilt, Metal-insulator transition and topological properties of pyrochlore iridates, Phys. Rev. Lett. **118**, 026404 (2017).

[9] K. Matsuhira, M. Wakeshima, Y. Hinatsu, and S. Takagi, Metal–insulator transitions in pyrochlore oxides $Ln_2Ir_2O_7$, J. Phys. Soc. Jpn. **80**, 094701 (2011).

[10] S. M. Disseler, C. Dhital, A. Amato, S. R. Giblin, C. de la Cruz, S. D. Wilson, and M. J. Graf, Magnetic order in the pyrochlore iridates $A_2Ir_2O_7$ (A = Y, Yb), Phys. Rev. B **86**, 014428 (2012).

[11] M. Graf, S. Disseler, C. Dhital, T. Hogan, M. Bojko, A. Amato, H. Luetkens, C. Baines, D. Margineda, S. Giblin, M. Jura, and S. Wilson, Magnetism and magnetic order in the pyrochlore iridates in the insulator-to-metal crossover region, J. Phys.: Conf. Ser. **551**, 012020 (2014).

[12] Y. Tokiwa, J. J. Ishikawa, S. Nakatsuji, and P. Gegenwart, Quantum criticality in a metallic spin liquid, Nat. Mater. **13**, 356 (2014).

[13] S. Nakatsuji, Y. Machida, Y. Maeno, T. Tayama, T. Sakakibara, J. van Duijn, L. Balicas, J. N. Millican, R. T. Macaluso, and J. Y. Chan, Metallic spin-liquid behavior of the geometrically frustrated kondo lattice $Pr_2Ir_2O_7$, Phys. Rev. Lett. **96**, 087204 (2006).

[14] T. Ohtsuki, Z. Tian, M. Halim, S. Nakatsuji, and M. Lippmaa, Growth of $Pr_2Ir_2O_7$ thin films using solid phase epitaxy, J. Appl. Phys. **127**, 035303 (2020).

[15] Y. Machida, S. Nakatsuji, S. Onoda, T. Tayama, and T. Sakakibara, Time-reversal symmetry breaking and spontaneous Hall effect without magnetic dipole order, Nature (London) **463**, 210 (2010).

[16] T. Kondo, M. Nakayama, R. Chen, J. J. Ishikawa, E.-G. Moon, T. Yamamoto, Y. Ota, W. Malaeb, H. Kanai, Y. Nakashima, Y. Ishida, R. Yoshida, H. Yamamoto, M. Matsunami, S. Kimura, N. Inami, K. Ono, H. Kumigashira, S. Nakatsuji, L. Balents, and S. Shin, Quadratic Fermi node in a 3D strongly correlated semimetal, Nat. Commun. **6**, 10042 (2015).

[17] B. Cheng, T. Ohtsuki, D. Chaudhuri, S. Nakatsuji, M. Lippmaa, and N. P. Armitage, Dielectric anomalies and interactions in the three-dimensional quadratic band touching Luttinger semimetal $Pr_2Ir_2O_7$, Nat. Commun. **8**, 2097 (2017).

[18] T. Ohta, A. Bostwick, T. Seyller, K. Horn, and E. Rotenberg, Controlling the electronic structure of bilayer graphene, Science **313**, 951 (2006).

[19] R. Wagner and A. Ewald, Free carrier reflectivity of gray tin single crystals, J. Phys. Chem. Solids **32**, 697 (1971).

[20] C. Brüne, C. X. Liu, E. G. Novik, E. M. Hankiewicz, H. Buhmann, Y. L. Chen, X. L. Qi, Z. X. Shen, S. C. Zhang, and L. W. Molenkamp, Quantum hall effect from the topological surface states of strained bulk HgTe, Phys. Rev. Lett. **106**, 126803 (2011).

[21] B. A. Bernevig, T. L. Hughes, and S.-C. Zhang, Quantum spin hall effect and topological phase transition in HgTe quantum wells, Science **314**, 1757 (2006).

[22] S. Zaheer, S. M. Young, D. Cellucci, J. C. Y. Teo, C. L. Kane, E. J. Mele, and A. M. Rappe, Spin texture on the Fermi surface of tensile-strained HgTe, Phys. Rev. B **87**, 045202 (2013).

[23] M. Kargarian, J. Wen, and G. A. Fiete, Competing exotic topological insulator phases in transition-metal oxides on the pyrochlore lattice with distortion, Phys. Rev. B **83**, 165112 (2011).

[24] P. Telang, K. Mishra, G. Prando, A. K. Sood, and S. Singh, Anomalous lattice contraction and emergent electronic phases in Bi-doped $Eu_2Ir_2O_7$, Phys. Rev. B **99**, 201112(R) (2019).

[25] P. Telang and S. Singh, Protracting the Weyl phase by a giant negative lattice expansion in Bi doped $Sm_2Ir_2O_7$, arXiv:2106.03512 (2021).

[26] A. Thomas, P. Telang, K. Mishra, M. Cesnek, J. Bednarcik, D. V. S. Muthu, S. Singh, and A. K. Sood, Role of spin-phonon and electron-phonon interactions in the phonon renormalization of $(Eu_{1-x}Bi_x)_2Ir_2O_7$ across the metal-insulator phase transition: Temperature-dependent Raman and x-ray studies, Phys. Rev. B **105**, 075145 (2022).

[27] M. Rosalin, P. Telang, S. Singh, D. V. S. Muthu, and A. K. Sood, Raman signatures of quadratic band touching state and strong spin-phonon coupling in pyrochlore iridates $(Sm_{1-x}Bi_x)_2Ir_2O_7$, Phys. Rev. B **108**, 035133 (2023).

[28] K. Ueda, R. Kaneko, A. Subedi, M. Minola, B. J. Kim, J. Fujioka, Y. Tokura, and B. Keimer, Phonon anomalies in pyrochlore iridates studied by Raman spectroscopy, Phys. Rev. B **100**, 115157 (2019).

[29] J. Son, B. C. Park, C. H. Kim, H. Cho, S. Y. Kim, L. J. Sandilands, C. Sohn, J.-G. Park, S. J. Moon, and T. W. Noh, Unconventional spin-phonon coupling via the Dzyaloshinskii–Moriya interaction, npj Quantum Mater. **4**, 17 (2019).

[30] D. J. Arenas, L. V. Gasparov, W. Qiu, J. C. Nino, C. H. Patterson, and D. B. Tanner, Raman study of phonon modes in bismuth pyrochlores, Phys. Rev. B **82**, 214302 (2010).

[31] D. Liang, H. Liu, N. Liu, L. Ling, Y. Han, L. Zhang, and C. Zhang, Structural, magnetic and electrical properties in the pyrochlore oxide $Bi_{2-x}Ca_xIr_2O_{7-\delta}$, Ceram. Int. **42**, 4562 (2015).

[32] H. Kumar, V. Sathe, and A. Pramanik, Spin-phonon coupling in hole-doped pyrochlore iridates $Y_2(Ir_{1-x}Ru_x)_2O_7$: A Raman scattering study, J. Magn. Magn. Mater. **478**, 148 (2019).

[33] Y. Xu, H. Man, N. Tang, T. Ohtsuki, S. Baidya, S. Nakatsuji, D. Vanderbilt, and N. Drichko, Phonon spectrum of $Pr_2Zr_2O_7$ and $Pr_2Ir_2O_7$ as evidence of coupling of the lattice with electronic and magnetic degrees of freedom, Phys. Rev. B **105**, 075137 (2022).

[34] P. Telang, K. Mishra, A. K. Sood, and S. Singh, Dilute stuffing in the pyrochlore iridate $Eu_2Ir_2O_7$, Phys. Rev. B **97**, 235118 (2018).

[35] H. Kumar, R. S. Dhaka, and A. K. Pramanik, Evolution of structure, magnetism, and electronic transport in the doped pyrochlore iridate $Y_2Ir_{2-x}Ru_xO_7$, Phys. Rev. B **95**, 054415 (2017).

[36] K. Kimura, Y. Ohta, and S. Nakatsuji, Structural, magnetic, and electrical properties in the metallic pyrochlore $Pr_{2+x}Ir_{2-x}O_{7+\delta}$, J. Phys.: Conf. Ser. **400**, 032040 (2012).

[37] Y. Machida, S. Nakatsuji, H. Tonomura, T. Tayama, T. Sakakibara, J. van Duijn, C. Broholm, and Y. Maeno, Crystalline electric field levels and magnetic properties of the metallic pyrochlore compound $Pr_2Ir_2O_7$, J. Phys. Chem. Solids **66**, 1435 (2005).

[38] See Supplemental Material at http://link.aps.org/supplemental/10.1103/PhysRevB.108.195144 for information on the sample synthesis, EDS and XPS data (Figs. S1 and S2), supporting figures for ERS (Figs. S3–S5), temperature evolution of E_g phonon and crystal field excitation (Fig. S6) and values of electron-phonon and phonon-phonon coupling strengths extracted from Eqs. (6)–(8) (table I).

[39] P. Telang, A. Bandyopadhyay, K. Mishra, D. Rout, R. Bag, A. Gloskovskii, Y. Matveyev, and S. Singh, en X-ray photoemission and absorption study of the pyrochlore iridates $(Eu_{1-x}Bi_x)_2Ir_2O_7$, $0 \leqslant x \leqslant 1$, J. Phys.: Condens. Matter **34**, 395601 (2022).

[40] M. Das, S. Bhowal, J. Sannigrahi, A. Bandyopadhyay, A. Banerjee, G. Cibin, D. Khalyavin, N. Banerjee, D. Adroja, I. Dasgupta, and S. Majumdar, Interplay between structural, magnetic, and electronic states in the pyrochlore iridate $Eu_2Ir_2O_7$, Phys. Rev. B **105**, 134421 (2022).

[41] M. S. Khan, I. Carlomagno, C. Meneghini, P. K. Biswas, F. Bert, S. Majumdar, and S. Ray, Mixed-valent metallic pyrochlore iridate: A possible route to non-Fermi liquids, Phys. Rev. B **105**, 085137 (2022).

[42] J. M. Kahk, C. G. Poll, F. E. Oropeza, J. M. Ablett, D. Céolin, J.-P. Rueff, S. Agrestini, Y. Utsumi, K. D. Tsuei, Y. F. Liao, F. Borgatti, G. Panaccione, A. Regoutz, R. G. Egdell, B. J. Morgan, D. O. Scanlon, and D. J. Payne, Understanding the electronic structure of IrO_2 using hard-X-ray photoelectron spectroscopy and density-functional theory, Phys. Rev. Lett. **112**, 117601 (2014).

[43] A. Kotani and Y. Toyozawa, Photoelectron spectra of core electrons in metals with an incomplete shell, J. Phys. Soc. Jpn. **37**, 912 (1974).

[44] P. A. Cox, R. G. Egdell, J. B. Goodenough, A. Hamnett, and C. C. Naish, The metal-to-semiconductor transition in ternary ruthenium (IV) oxides: A study by electron spectroscopy, J. Phys. C **16**, 6221 (1983).

[45] G. K. Wertheim and H. J. Guggenheim, Conduction-electron screening in metallic oxides: IrO_2, Phys. Rev. B **22**, 4680 (1980).

[46] M. Y. A. Yagoub, H. C. Swart, P. Bergman, and E. Coetsee, Enhanced Pr^{3+} photoluminescence by energy transfer in SrF_2 : Eu^{2+}, Pr^{3+} phosphor, AIP Adv. **6**, 025204 (2016).

[47] A. J. Princep, D. Prabhakaran, A. T. Boothroyd, and D. T. Adroja, Crystal-field states of Pr^{3+} in the candidate quantum spin ice $Pr_2Sn_2O_7$, Phys. Rev. B **88**, 104421 (2013).

[48] M. L. Sanjuán, C. Guglieri, S. Díaz-Moreno, G. Aquilanti, A. F. Fuentes, L. Olivi, and J. Chaboy, Raman and x-ray absorption spectroscopy study of the phase evolution induced by mechanical milling and thermal treatments in $R_2Ti_2O_7$ pyrochlores, Phys. Rev. B **84**, 104207 (2011).

[49] C. L. Tracy, J. Shamblin, S. Park, F. Zhang, C. Trautmann, M. Lang, and R. C. Ewing, Role of composition, bond covalency, and short-range order in the disordering of stannate pyrochlores by swift heavy ion irradiation, Phys. Rev. B **94**, 064102 (2016).

[50] A. A. Abrikosov, Calculation of critical indices for zero-gap semiconductors, Sov. Phys. JETP **39**, 709 (1974).

[51] K. Sen, D. Fuchs, R. Heid, K. Kleindienst, K. Wolff, J. Schmalian, and M. Le Tacon, Strange semimetal dynamics in $SrIrO_3$, Nat. Commun. **11**, 4270 (2020).

[52] S. L. Cooper, F. Slakey, M. V. Klein, J. P. Rice, E. D. Bukowski, and D. M. Ginsberg, Gap anisotropy and phonon self-energy effects in single-crystal $YBa_2Cu_3O_{7-\delta}$, Phys. Rev. B **38**, 11934 (1988).

[53] M. Opel, R. Nemetschek, C. Hoffmann, R. Philipp, P. F. Müller, R. Hackl, I. Tüttő, A. Erb, B. Revaz, E. Walker, H. Berger, and L. Forró, Carrier relaxation, pseudogap, and superconducting gap in high-T_c cuprates: A Raman scattering study, Phys. Rev. B **61**, 9752 (2000).

[54] X. K. Chen, E. Altendorf, J. C. Irwin, R. Liang, and W. N. Hardy, Oxygen-concentration dependence of the Raman continua in $YBa_2Cu_3O_y$ single crystals, Phys. Rev. B **48**, 10530 (1993).

[55] F. Kretzschmar, T. Böhm, U. Karahasanović, B. Muschler, A. Baum, D. Jost, J. Schmalian, S. Caprara, M. Grilli, C. di Castro, J. G. Analytis, J. H. Chu, I. R. Fisher, and R. Hackl, Critical spin fluctuations and the origin of nematic order in $Ba(Fe_{1-x}Co_x)_2As_2$, Nat. Phys. **12**, 560 (2016).

[56] U. Nagel, T. Uleksin, T. Rõõm, R. P. S. M. Lobo, P. Lejay, C. C. Homes, J. S. Hall, A. W. Kinross, S. K. Purdy, T. Munsie, T. J. Williams, G. M. Luke, and T. Timusk, Optical spectroscopy shows that the normal state of URu_2Si_2 is an anomalous Fermi liquid, Proc. Natl. Acad. Sci. USA **109**, 19161 (2012).

[57] P. E. Sulewski, A. J. Sievers, M. B. Maple, M. S. Torikachvili, J. L. Smith, and Z. Fisk, Far-infrared absorptivity of UPt_3, Phys. Rev. B **38**, 5338 (1988).

[58] D. Stricker, J. Mravlje, C. Berthod, R. Fittipaldi, A. Vecchione, A. Georges, and D. van der Marel, Optical response of Sr_2RuO_4 reveals universal fermi-liquid scaling and quasiparticles beyond landau theory, Phys. Rev. Lett. **113**, 087404 (2014).

[59] K. Wang, B. Xu, C. W. Rischau, N. Bachar, B. Michon, J. Teyssier, Y. Qiu, T. Ohtsuki, B. Cheng, N. P. Armitage, S. Nakatsuji, and D. v. d. Marel, Unconventional free charge

[59] in the correlated semimetal $Nd_2Ir_2O_7$, Nat. Phys. **16**, 1194 (2020).

[60] W. Götze and P. Wölfle, Homogeneous dynamical conductivity of simple metals, Phys. Rev. B **6**, 1226 (1972).

[61] A. Tytarenko, Y. Huang, A. de Visser, S. Johnston, and E. van Heumen, Direct observation of a Fermi liquid-like normal state in an iron-pnictide superconductor, Sci. Rep. **5**, 12421 (2015).

[62] O. Vafek and K. Yang, Many-body instability of Coulomb interacting bilayer graphene: Renormalization group approach, Phys. Rev. B **81**, 041401(R) (2010).

[63] U. Fano, Effects of configuration interaction on intensities and phase shifts, Phys. Rev. **124**, 1866 (1961).

[64] T. M. H. Nguyen, L. J. Sandilands, C. H. Sohn, C. H. Kim, A. L. Wysocki, I.-S. Yang, S. J. Moon, J.-H. Ko, J. Yamaura, Z. Hiroi, and T. W. Noh, Two-magnon scattering in the 5d all-in-all-out pyrochlore magnet $Cd_2Os_2O_7$, Nat. Commun. **8**, 251 (2017).

[65] B. Xu, Y. M. Dai, L. X. Zhao, K. Wang, R. Yang, W. Zhang, J. Y. Liu, H. Xiao, G. F. Chen, S. A. Trugman, J.-X. Zhu, A. J. Taylor, D. A. Yarotski, R. P. Prasankumar, and X. G. Qiu, Temperature-tunable Fano resonance induced by strong coupling between Weyl fermions and phonons in TaAs, Nat. Commun. **8**, 14933 (2017).

[66] N. Martin, P. Bonville, E. Lhotel, S. Guitteny, A. Wildes, C. Decorse, M. Ciomaga Hatnean, G. Balakrishnan, I. Mirebeau, and S. Petit, Disorder and quantum spin Ice, Phys. Rev. X **7**, 041028 (2017).

[67] M. Ju, X. Kuang, C. Lu, H. Li, J. Wang, C. Zhang, Y. Zhu, and Y. Yeung, Determination of the microstructure, energy levels and magnetic dipole transition mechanism for Tm^{3+} doped yttrium aluminum borate, J. Mater. Chem. C **4**, 1988 (2016).

[68] P. Bonville, S. Guitteny, A. Gukasov, I. Mirebeau, S. Petit, C. Decorse, M. C. Hatnean, and G. Balakrishnan, Magnetic properties and crystal field in $Pr_2Zr_2O_7$, Phys. Rev. B **94**, 134428 (2016).

[69] Y. Xu, H. Man, N. Tang, S. Baidya, H. Zhang, S. Nakatsuji, D. Vanderbilt, and N. Drichko, Importance of dynamic lattice effects for crystal field excitations in the quantum spin ice candidate $Pr_2Zr_2O_7$, Phys. Rev. B **104**, 075125 (2021).

[70] J. A. Sanjurjo, C. Rettori, S. Oseroff, and Z. Fisk, Raman-scattering study of crystal-field excitations in Pr_2CuO_4, Phys. Rev. B **49**, 4391 (1994).

[71] R. Orbach, Spin-lattice relaxation in rare-earth salts, Proc. R. Soc. London Ser., A **264**, 458 (1961).

[72] S. Huefner, *Optical Spectra of Transparent Rare Earth Compounds* (Academic Press, New York, 1978).

[73] P. G. Klemens, Anharmonic decay of optical phonons, Phys. Rev. **148**, 845 (1966).

[74] H.-N. Liu, X. Cong, M.-L. Lin, and P.-H. Tan, The intrinsic temperature-dependent Raman spectra of graphite in the temperature range from 4 K to 1000 K, Carbon **152**, 451 (2019).

[75] N. Bonini, M. Lazzeri, N. Marzari, and F. Mauri, Phonon anharmonicities in graphite and graphene, Phys. Rev. Lett. **99**, 176802 (2007).

[76] H. Takatsu, K. Watanabe, K. Goto, and H. Kadowaki, Comparative study of low-temperature x-ray diffraction experiments on $R_2Ir_2O_7$ (R = Nd, Eu, and Pr), Phys. Rev. B **90**, 235110 (2014).

[77] A. Sethi, J. E. Slimak, T. Kolodiazhnyi, and S. L. Cooper, Emergent vibronic excitations in the magnetodielectric regime of Ce_2O_3, Phys. Rev. Lett. **122**, 177601 (2019).

[78] E. T. Heyen, R. Wegerer, E. Schönherr, and M. Cardona, Raman study of the coupling of crystal-field excitations to phonons in $NdBa_2Cu_3O_{7-\delta}$, Phys. Rev. B **44**, 10195 (1991).

[79] J. Gaudet, A. M. Hallas, C. R. C. Buhariwalla, G. Sala, M. B. Stone, M. Tachibana, K. Baroudi, R. J. Cava, and B. D. Gaulin, Magnetoelastically induced vibronic bound state in the spin-ice pyrochlore $Ho_2Ti_2O_7$, Phys. Rev. B **98**, 014419 (2018).

[80] F. Ishii, Y. P. Mizuta, T. Kato, T. Ozaki, H. Weng, and S. Onoda, First-principles study on cubic pyrochlore iridates $Y_2Ir_2O_7$ and $Pr_2Ir_2O_7$, J. Phys. Soc. Jpn. **84**, 073703 (2015).